Magnetic investigations on irradiation-induced nanoscale precipitation in reactor pressure vessel steels: A first-order reversal curve study

Satoru Kobayashi[a,*], Hiroaki Murakami[a], Takuya Yamamoto[b], G. Robert Odette[b], Ákos Horváth[c], Artem Feoktystov[d], László Almásy[c]

[a] *Faculty of Science and Engineering, Iwate University, Ueda 4-3-5, Morioka 020-8551, Japan*
[b] *Department of Mechanical and Environmental Engineering, University of California Santa Barbara, Santa Barbara, CA 93106, USA*
[c] *Centre for Energy Research, Hungarian Academy of Sciences, H-1525 Budapest 114, Hungary*
[d] *Forschungszentrum Jülich GmbH, Jülich Centre for Neutron Science (JCNS) at Heinz Maier-Leibnitz Zentrum (MLZ), 85748 Garching, Germany*

Abstract

We have investigated magnetic properties for reactor pressure vessel model alloys with variable Cu contents, subjected to neutron irradiation up to a fluence of 9×10^{19} n cm^{-2}. Unlike a monotonic increase of microhardness with neutron fluence, the major-loop coercivity decreases at a higher fluence and the decrease becomes larger for the alloy containing a higher amount of Cu. The measurements of first-order reversal curves (FORCs) for the high-Cu alloy show that the position of the FORC distribution peak shifts toward a lower coercivity just after neutron irradiation, followed by a slight increase, associated with the broadening along both the coercivity and interaction field axes. The results can be explained by the enhancement of magnetic inhomogeneity in a matrix due to Cu precipitation and an increasing magnetostatic interaction between local magnetic regions with different coercivity. The magnetic method using FORCs can be a possible technique which provides in-depth information on microstructural changes due to neutron irradiation, which is not obtained by measurements of a conventional major hysteresis loop.

Keywords: Neutron irradiation, Magnetic hysteresis, SANS, First-order-reversal curves, Pressure vessel

1. Introduction

Reactor pressure vessel (RPV) is the major safety-critical component in a light water reactor (LWR) plant. During the operation at the service temperature of ~ 290 °C, a RPV,

*Corresponding author
Email address: koba@iwate-u.ac.jp (Satoru Kobayashi)

which is made of low-alloy steels, is subjected to irradiation by high-energy neutrons, yielding the embrittlement [1]. For the long-term safety operation, the embrittlement should be appropriately evaluated and predicted. The irradiation-induced embrittlement of RPV steels is primarily caused by both precipitation and defect hardening; Cu-rich precipitation contributes to the hardening in low and medium fluence regimes, whereas the Mn-Ni-Si-enriched precipitates dominate the hardening at high fluence [1, 2]. Currently, the embrittlement is evaluated by a ductile-to-brittle transition temperature (DBTT) shift, which is obtained by a Charpy impact test of surveillance Charpy samples preinstalled in a RPV. However, most of the samples were withdrawn in the designed lifetime of RPVs and the diminishing stock is a crucial issue.

Non-destructive evaluation (NDE) methods have the potential for monitoring the level of the irradiation embrittlement during service. Their development is critically important, because the integrity of RPVs can be assessed over a long period of time using the same irradiated surveillance samples [3, 4]. Since RPV steels used for LWR plants are ferromagnetic, a magnetic method using hysteresis loops has been considered to be one of useful NDE methods to evaluate the microstructural changes; lattice defects create a stress field and can act as pinning centers to the movement of magnetic domain walls [5], resulting in a change in hysteresis properties depending on the level of microstructural changes [6, 7]. Historically, coercivity and remanence of the major hysteresis loops have been mainly focused on to seek irradiation effect on RPV steels [8, 9, 10, 11]. Extensive investigations revealed that coercivity and remanence change after neutron irradiation; however, the results strongly depend on experimental conditions and the irradiation effect has been controversial. In the last two decades, we have focused on minor hysteresis loops, because a minor-loop coefficient is sensitive to defect density and obtained with low applied fields [12, 13]. We found that the coefficient changes with neutron fluence and increases with Cu, Ni, and Mn contents which are key elements for irradiation hardening [14, 15, 16]. However, the coefficient exhibits a local maximum in the low-to-medium fluence regime, whereas DBTT and hardening-sensitive properties like yield stress, hardness, increase monotonically with fluence [1]. The observed local maximum was explained as due to competing microstructural changes; the increasing density of Cu-rich precipitates increases the coefficient, whereas the recovery through such as rearrangement of dislocations decreases it. The relatively higher sensitivity of magnetic properties to recovery makes it difficult to extract the information about precipitation hardening from magnetic hysteresis properties [16].

A magnetic method using first-order-reversal curves (FORCs) may be useful to investigate ferromagnetic materials with complicated microstructures [17, 18, 19, 20]. FORCs are one types of minor loops and magnetization at the same magnetic field is measured by several different histories, which enable us to provide valuable information about coercivity distribution and local interaction field. Quite recent studies on Nd-Fe-B sintered magnets [18] and multi-phase materials [19] showed that magnetic features with different microstructural origin can be successfully separated in the FORC diagram, unlike a major hysteresis loop that reflects an average of microstructures. In this paper, we report results of major hysteresis and FORC measurements for neutron-irradiated RPV model alloys with variable Cu contents to get in-depth information on their microstructural changes after neutron

Table 1: Chemical compositions of measured samples. (wt%)

Sample	Cu	Ni	Mn	Cr	Mo	P	C	Si
LG	0.00	0.74	1.37	0.05	0.55	0.005	0.16	0.22
LH	0.11	0.74	1.39	0.05	0.55	0.005	0.16	0.24
LJ	0.42	0.81	1.34	0.085	0.55	0.005	0.16	0.13

Table 2: Neutron irradiation conditions

	Flux (>1 MeV) (10^{13} n cm^{-2}s^{-1})	Fluence (>1 MeV) (10^{19} n cm^{-2})	Irradiation exposure time (days)
Irrad-1	1.46	0.19	1.4
Irrad-2	1.44	0.55	4.2
Irrad-3	2.12	2.99	16
Irrad-4	2.15	9.15	49

irradiation.

2. Experimental

Three A533B-type RPV model alloys with different chemical compositions were used as listed in Table 1. The LG sample has no Cu content, whereas LH and LJ have medium (0.11%) and high (0.42%) Cu content, respectively, with keeping Ni and Mn contents nearly constant. The alloys were austenitized at 900°C for 1 h, air cool, tempered at 664°C for 4 h, air cool, stress relieved at 600°C for 40 h, furnace cooled to 300°C, and air cooled. The microstructure of the as-received (AR) sample is a mixed tempered ferrite-bainite structure. The detail of the model alloys is given in literatures [21].

Small plate samples with dimensions of 2 × 12 × 0.5 mm^3 were neutron-irradiated at 300°C to fluences up to 9.15 × 10^{19} n cm^{-2} (> 1 MeV) in the BR2 reactor at SCK·CEN in Belgium. To obtain samples with four different neutron irradiation condition, the irradiation was performed in four needles with subcapsules that contain the samples under helium atmosphere. Each needle experienced a different irradiation fluence because the needles were lifted out after different irradiation time. The temperature of subcapsules was precisely controlled with electrical heaters and monitored with thermocouples. The average temperature during neutron irradiation was 300±1 °C. The neutron flux and fluence were calculated based on results of dosimetry measurements using Fe dosimeters, which are listed in Table 2. For each alloy and irradiation condition, two samples were prepared.

Microhardness was measured with a load of 300 gf and the averaged value was obtained from approximately 20 indents for each irradiation condition.

Small-angle neutron scattering (SANS) measurements were performed, at the Heinz

Maier-Leibnitz Zentrum (MLZ), Garching, Germany, using the KWS-1 SANS instrument [22, 23]. The small plate samples with dimensions of 2 × 12 × 0.5 mm^3, were used. The wavelength of neutrons was 5.0 Å and two dimensional (2D) detector position was set at three different sample-detector distances of 1.5, 8.0, and 20 m, covering a scattering vector Q in the range from 0.002 to 0.3 $Å^{-1}$. In order to separate magnetic and nuclear contributions, a vertical magnetic field of 2.2 T, which is enough to saturate the sample, was applied along the direction perpendicular to the neutron beam. The SANS intensities due to magnetic contrast were analyzed with an analysis tool developed by Ilavsky et al. [24]

Magnetic measurements were carried out at room temperature using a fluxmeter designed for neutron-irradiated small samples [16]. A U-shape Fe-Si yoke was attached to a sample surface to form a closed magnetic circuit. A 500-turn excitation coil was wound around the yoke and the triangular current was applied to the coil to generate magnetic field inside the sample. Induced voltages, detected by a 400-turn pick-up coil, were used to obtain the magnetic flux inside the sample. Measured voltages were converted to digital signals by the AD converter with a sampling frequency of $\sim 10^5$ Hz. After the signal processing, a magnetic-flux-density (B)-vs-field (H) hysteresis loop was obtained. The detail of the measurement setup is described in Ref. 16.

FORCs with different reversal fields, H_r, were measured at a field sweep rate of dH/dt = 18 kA/m/s; magnetic field, H, is reduced from a saturation field of 14 kA/m and then increases toward 14 kA/m after H reaches H_r. This procedure was repeated with reducing H_r with a step of $\sim$ 280 A/m. The FORCs are a function of H_r and H, and FORC distribution is defined as

$$\rho(H, H_r) = -\frac{1}{2}\frac{\partial^2 B(H, H_r)}{\partial H \partial H_r}. \quad (1)$$

FORC diagrams were plotted by using rotating axes; an interaction field axis $H_u = (H + H_r)/2$ and a coercivity axis $H_c = (H - H_r)/2$. Generally, the intensity of $\rho(H_c, H_u)$ is related to irreversibility at given H_c and H_u [17].

All the measurements were performed for samples separately prepared for different irradiation condition. Since magnetic properties are sensitive to initial microstructure as compared to hardness, samples which had almost the same coercivity before irradiation were only used for the measurements. The averaged coercivity for as-received LG, LH, and LJ samples was 745 ± 8, 798 ± 14, and 787 ± 6, respectively; the percentage of deviation from the average was 1.0, 1.7, and 0.7 %, respectively.

For each irradiation and alloy condition, two samples were measured and the magnetic parameters such as coercivity and FORC parameters were averaged. The experimental error of the magnetic parameters was found to mainly result from the sample dependence and the error bars of the magnetic parameters are standard deviation of the averaged values for the two samples.

Note the influence of contact between sample surface and U-shape yoke on hysteresis parameters. When the contact is not complete due to such as incomplete flatness of the sample surface, measured hysteresis loop was slightly inclined and the remanence becomes lower, whereas coercivity was not sensitive to the contact condition. In the case of coercivity

measurements from the major loop, therefore, we did not pay close attention to the perfect contact condition. Therefore, there is no systematic relationship between coercivity and remanence changes due to neutron irradiation. On the other hand, in the case of FORCs, such incomplete contact yielded a broadening of FORC distribution curve [20]. Therefore, in the case of FORC measurements, a great care was taken for the contact.

3. Experimental results and discussions

3.1. Vickers hardness

Figure 1 shows a change of Vickers hardness for LG, LH, and LJ samples, as a function of neutron fluence. Vickers hardness before neutron irradiation was 196 ± 6, 196 ± 7, and 202 ± 6 for LG, LH, LJ samples, respectively, and slightly depends on chemical compositions [21]. For all the sample hardness increases with neutron fluence, and the larger increase of hardness was observed for the high-Cu sample. This reflects the higher volume fraction of Cu-rich precipitates for Cu-bearing alloy (LH, LJ; Cu $\geq\approx$ 0.07 wt%), as commonly observed in previous studies [1]. In the case of the Cu-free LG sample, the increase of the hardness with neutron fluence would be mainly caused by matrix features such as solute-vacancy complexes.

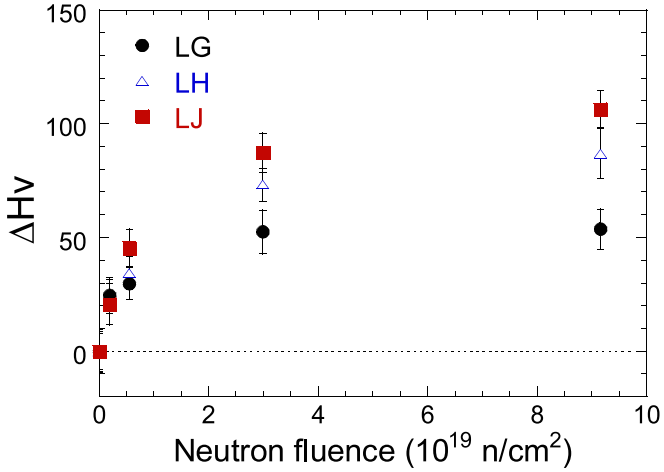

Figure 1: Change of hardness as a function of neutron fluence. The circles, triangles, and squares represent data for LG, LH, and LJ, respectively.

3.2. SANS measurements

To investigate irradiation-induced nanoscale features, we performed SANS measurements for the LG, LH, and LJ samples in the four irradiation conditions listed in Table 2. For all the samples, we observed butterfly patterns of SANS intensity in the 2D detector, reflecting

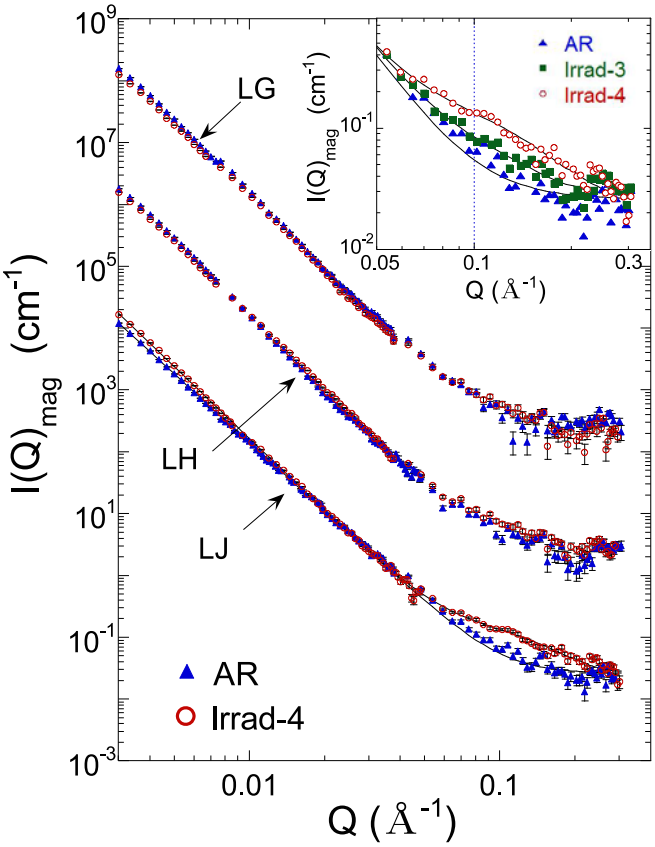

Figure 2: Magnetic SANS intensities in the AR and Irrad-4 conditions. The inset shows the enlargement around $Q \sim 0.1\text{Å}^{-1}$ for LJ, with different irradiation condition. The solid lines through the data for the LJ sample are the least-squares fitting lines.

strong magnetic scattering due to a Fe matrix In a saturated state, SANS intensity, $I(Q)$ is given by

$$I(Q) = I(Q)_{\text{nuc}} + I(Q)_{\text{mag}}\sin^2\theta, \tag{2}$$

where θ is the angle between Q vector and applied magnetic field in the detector plane, $I(Q)_{\text{nuc}}$ and $I(Q)_{\text{mag}}$ are nuclear and magnetic SANS intensities, respectively [25, 26]. $I(Q)_{\text{mag}}$ was obtained by subtracting $I(Q)$ for $\theta = 0°$ from that for $\theta = 90°$.

Figure 2 shows $I(Q)_{\text{mag}}$ curves for the LG, LH, and LJ samples for the AR and Irrad-4 conditions. For the LG and LH samples with no and low Cu contents, respectively, there is no discernible difference before and after the irradiation within accuracy of our measurements. In the case of the LJ sample with a high Cu content, on the other hand, $I(Q)_{\text{mag}}$ exhibits a significant increase and broad peak at around $Q = 0.1$ Å^{-1} after the irradiation as shown in the inset in Fig. 2. This suggests the development of nanoscale features for the LJ sample, yielding magnetic contrast between the matrix and nanoscale features.

Table 3: Parameters of nanoscale features for LJ, obtained from SANS

	Fluence (>1 MeV) (10^{19} n cm^{-2})	Radius (nm)	Volume fraction (%)	Number density (cm^{-3})
Irrad-3	2.99	1.6	0.11	6.6×10^{16}
Irrad-4	9.15	1.5	0.37	2.7×10^{17}

To extract the detailed microstructural information from $I(Q)_{\mathrm{mag}}$, $I(Q)_{\mathrm{mag}}$ was least-squares fitted, assuming that nanoscale features are non-magnetic spheres with the log-normal size distribution [26]. In the fitting procedure, the background parameter obtained from the AR data was used for the irradiated samples to obtain reliable fitting parameters. Note that due to the small sample size, the SANS intensity at around $Q = 0.1$ Å^{-1}, which reflects the formation of nanoscale features, was not so intense as compared with the background and experimental errors; therefore, only the data for the high-fluence Irrad-3 and Irrad-4 conditions of the LJ sample, could be reliably fitted. In Table 3, parameters of nanoscale features for the LJ sample are summarized. The radius of nanoscale features is 1.5−1.6 nm for both conditions, and the volume fraction and number density for the Irrad-4 condition are approximately 3−4 times larger than that for the Irrad-3 condition.

During neutron irradiation, various kinds of nanoscale defects including Cu-rich precipitates, Mn-Ni-Si-enriched precipitates, small vacancy-type clusters, are formed [1, 2, 27]. In the case of Cu-bearing alloys (LH, LJ), the formation of nanoscale Cu-rich precipitates dominates irradiation hardening in the low-to-medium fluence regime. At the high fluence, Mn-Ni-Si-enriched precipitation additionally starts to influence the irradiation hardening. In our irradiation condition, neutron flux was 1.4−2.2 $\times10^{13}$ n cm^{-2}s^{-1} and approximately 20 times higher than that in our previous studies [14, 15, 16]. Generally, neutron flux influences nucleation and growing process of irradiation-induced defects and high flux results in delaying precipitation formation [1, 27, 28]. According to the analysis of flux effects on precipitation based on previous studies [1, 27], dominant nanoscale features for the Cu-bearing alloy (LH, LJ) are Cu-rich precipitates within our irradiation condition and full precipitation is achieved for the Irrad-4 condition; 0.1 and 0.4 % fraction for LH and LJ, respectively. The volume fraction listed in Table 3 is consistent with previous SANS and atom probe tomography studies [1, 26].

3.3. Magnetic measurements

Figures 3(a) and 3(b) show the major hysteresis loop for the LG and LJ samples, respectively, in the AR and Irrad-4 conditions. The insets show the enlarged view at low fields. For both samples, the loop width becomes slightly narrower after the irradiation, without significant modification in the overall loop shape. A change of major-loop coercivity, $\Delta H_{\mathrm{m,c}}$, as a function of neutron fluence is summarized in Fig. 4. Here, $\Delta H_{\mathrm{m,c}}$ for each irradiation condition was obtained by measuring the identical sample before and after the irradiation to obtain the coercivity change precisely. For comparison, a change of coercivity expected by

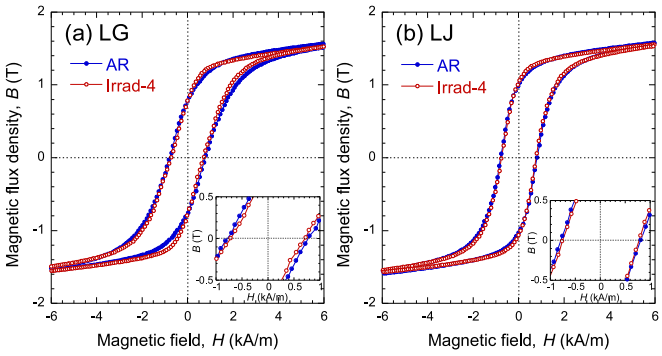

Figure 3: Major hysteresis loops in the AR and Irrad-4 conditions for (a) LG and (b) LJ. The insets show the enlargement around the origin. The solid and open circles denote data for the AR and Irrad-4 conditions, respectively. The experimental error of each data point is much smaller than the size of the symbols.

a thermal aging at ~ 300°C is also given for each sample. Here, this change was calculated using coercivity-vs-time data for thermal aging at 290°C [29] and the irradiation exposure time of each irradiation condition listed in Table 2, assuming that thermal aging effects at 290 and 300°C are almost the same [29]. For the LG and LH samples $\Delta H_{\mathrm{m,c}}$ drops just after the irradiation, exhibits a maximum at $\sim 1 \times 10^{19}$ n cm^{-2}, followed by the decrease with fluence, whereas that for the LJ sample maximizes just after the irradiation and then decreases with neutron fluence. The appearance of a maximum in $\Delta H_{\mathrm{m,c}}$ can be attributed to a competing effect of Cu precipitation and recovery, which result in an increase and decrease in coercivity, respectively [16]. Since the increasing effect for coercivity is enhanced for alloy with a high Cu content, the coercivity maximum for the LJ sample is located at a lower fluence than that for the LH and LG samples, being consistent with our previous study [16]. At the highest fluence (Irrad-4), the decrease of coercivity, as compared with the value before the irradiation, is 1.1, 2.0, and 2.0% for the LG, LH, and LJ samples, respectively. This indicates that the contribution of recovery to magnetic property changes is more significant than that of nanoscale defect formation at the highest fluence. For all the samples, the coercivity decrease is larger than that estimated by a thermal aging effect, primarily due to an enhanced recovery through radiation-induced diffusion process [1]. Considering almost the same values of $\Delta H_{\mathrm{m,c}}$ for the LJ and LH samples despite the higher contribution of Cu precipitation to a coercivity increase for the LJ sample, the recovery contribution can be more significant for the LJ sample than that for the LH sample. The observed fluence dependence of coercivity is in contrast to a behavior of Vickers hardness shown in Fig. 1 which is dominantly sensitive to nanoscale defect formation.

Figure 5 shows FORC diagrams for the LJ sample in the AR and Irrad-4 conditions. In the insets FORCs for each condition are given. In this study, we focused only on the LJ sample, which exhibits a significant irradiation effect on both hardness and $H_{\mathrm{m,c}}$. The FORC diagram has a single distribution peak on the H_{c} axis for all the irradiation conditions. The peak position slightly shifts toward a lower H_{c} after neutron irradiation.

To quantitatively analyze the FORC distribution peak, both the coercivity distribution,

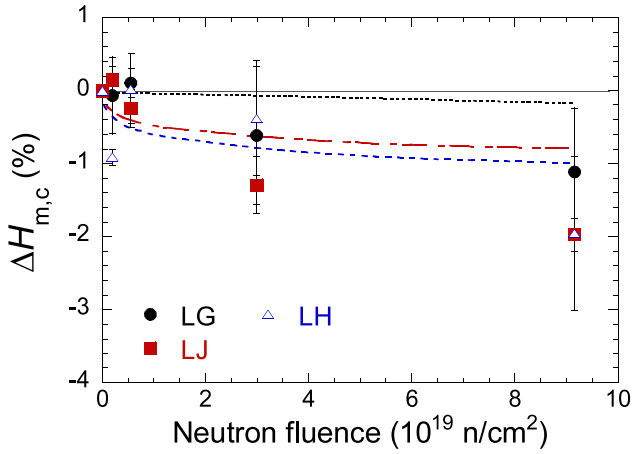

Figure 4: Change of major-loop coercivity, as a function of neutron fluence. The circles, triangles, and squares represent data for LG, LH, and LJ, respectively. The dotted, dashed, and dash-dotted lines denote a coercivity change due to thermal aging effect, estimated from previous thermal aging study [29].

$\rho_c(H_c)$, and the interaction field distribution, $\rho_u(H_u)$, were calculated using the following equations.

$$\rho_c(H_c) = \int_{-\infty}^{\infty} \rho(H_c, H_u) dH_u \tag{3}$$

$$\rho_u(H_u) = \int_{0}^{\infty} \rho(H_c, H_u) dH_c \tag{4}$$

Figures 6(a) and 6(b) show $\rho_c(H_c)$ and $\rho_u(H_u)$ for the LJ sample, respectively, in the AR and Irrad-4 condition. For $\rho_c(H_c)$, the peak is asymmetric in shape and becomes narrower after neutron irradiation. On the other hand, the $\rho_u(H_u)$ peak is located at $H_u \sim 0$ and seems to slightly become broad after the irradiation. To evaluate the position and width of the $\rho_c(H_c)$ and $\rho_u(H_u)$ peaks, $\rho_c(H_c)$ and $\rho_u(H_u)$ peaks were least-squares fitted assuming a lognormal distribution function and Lorentzian function, respectively.

Figures 7(a) and 7(b) show the peak position of $\rho_c(H_c)$, $H_{c,p}$, and the width parameter $\sigma_{c,p}$, respectively. The behavior of $\rho_c(H_c)$ peak gives information about coercivity distribution. As shown in Fig. 7(a), $H_{c,p}$ drops just after neutron irradiation, followed by a broad local maximum at around the medium fluence of $\sim 3 \times 10^{19}$ n cm^{-2}. Such a local maximum was observed in our previous study of the minor-loop coefficient for the LJ sample [16], and reflects competing microstructural changes of Cu-rich precipitation and recovery. Note that in the case of $H_{m,c}$ shown in Fig. 4, a slight increase just after neutron irradiation might reflect such a competition. On the other hand, $\sigma_{c,p}$ slightly increases ($\sim 3\%$) and then decreases at a higher fluence. This implies that the number of magnetic regions with different coercivity increases in the early stage of neutron irradiation. The decrease of $H_{c,p}$ and increase of $\sigma_{c,p}$ observed after the neutron irradiation is $\sim 3\%$ of the value of the AR samples, and is comparable to a change of $H_{m,c}$. Figures 7(c) and 7(d) show the peak

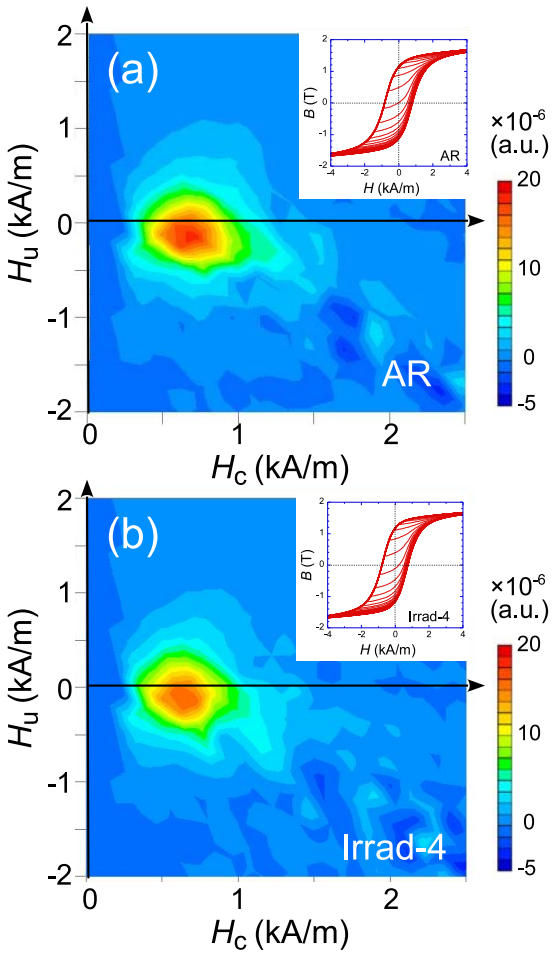

Figure 5: FORC diagrams for LJ in the (a) AR and (b) Irrad-4 conditions. The insets show the measured FORCs.

position of $\rho_{\mathrm{u}}(H_{\mathrm{u}})$, $H_{\mathrm{u,p}}$, and the half-width at half-maximum, $W_{\mathrm{u,p}}$, respectively. Whereas $H_{\mathrm{u,p}}$ seems to decrease and then increase with fluence, $W_{\mathrm{u,p}}$ exhibits an increase after the neutron irradiation; the changes of $H_{\mathrm{u,p}}$ and $W_{\mathrm{u,p}}$ for the Irrad-3 sample is $\sim 11\%$ and 4% of the value for the AR sample, respectively. These behavior implies the enhancement of interaction fields between magnetic units with different coercivity [17].

It should be noted that in our previous FORC study for other RPV model alloys including Russian-type RPV steels, only the data for $H_{\mathrm{c,p}}$ and $\sigma_{\mathrm{c,p}}$, which exhibits a decreasing trend with neutron fluence, was observed; this could be due to the shortage of data points in the low fluence regime and also due to lower Cu content (≤ 0.14 wt%Cu) [20]. Further, interaction-field parameters of $H_{\mathrm{u,p}}$ and $W_{\mathrm{u,p}}$ were not precisely obtained primarily due to a poor contact between the sample surface and Fe-Si yoke; this contact condition yielded the small air gap and a hysteresis loop was slightly sheared by the demagnetizing field inside the sample, resulting in an artificial broadening in $W_{\mathrm{u,p}}$. In this study, the contact condition

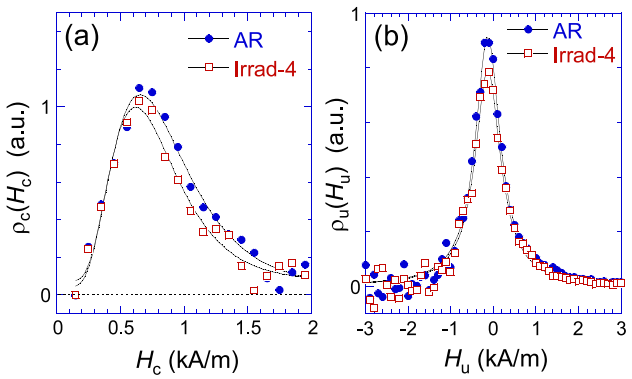

Figure 6: FORC distribution curves along (a) H_c and (b) H_u axes for LJ in the AR and Irrad-4 conditions.

was largely improved by carefully attaching the yoke to nearly flat surface.

Neutron irradiation induces the formation of various types of nanoscale defects such as Cu-rich precipitates, Mn-Ni-Si-dominated precipitates, dislocation loops, solute-vacancy complexes [1]. For the Cu-bearing LH and LJ samples, Cu-rich precipitation is a primary cause of irradiation hardening in our irradiation condition as described in Sec. 3.2. The volume fraction and size of Cu-rich precipitates develop with neutron fluence through radiation enhanced diffusion and segregation. Matrix features such as solute-vacancy complexes may also be formed during the irradiation, yielding steady but small hardening with fluence [1]. At the same time, irradiation-induced diffusion may accelerate recovery process through such as annihilation and rearrangement of pre-existing dislocations, which were produced during the manufacturing process. This reduces dislocation density in the matrix.

In ferromagnetic materials, magnetization process occurs primarily due to the displacement of Bloch walls which separate two magnetic domains with opposite magnetization [5]. Both nanoscale precipitates and dislocations create internal stress fields around them, resulting in the pinning of Bloch walls. This pinning will lead to an increase of $H_{\mathrm{m,c}}$ and $H_{\mathrm{c,p}}$. However, a Bloch wall width is a few tens nanometers ($\sim$ 40 nm for α-Fe) and is relatively wider than the size of nanoscale precipitates. Therefore, magnetic properties are more sensitive to internal stress due to dislocations than to nanoscale precipitates, unlike mechanical properties such as hardness and yield stress that are sensitive to nanoscale features [30, 31]. During neutron irradiation, the nanoscale defect formation and recovery occur simultaneously for the Cu-bearing samples. The former increases $H_{\mathrm{m,c}}$ and $H_{\mathrm{c,p}}$ whereas the latter decreases them. For the LJ sample with a higher Cu content, effects of the precipitate formation are further enhanced as compared with the LH and LG samples. The local maximum in $H_{\mathrm{c,p}}$ at around $\sim 3 \times 10^{19}$ n cm^{-2} (Fig. 7(a)) and possibly in a slight increase of $H_{\mathrm{m,c}}$ just after irradiation (Fig. 4) may reflect the competition between the precipitation and recovery.

The precipitation formation also influences other FORC parameters for the LJ sample and this can be explained as follows. Before neutron irradiation, all Cu atoms are dissolved

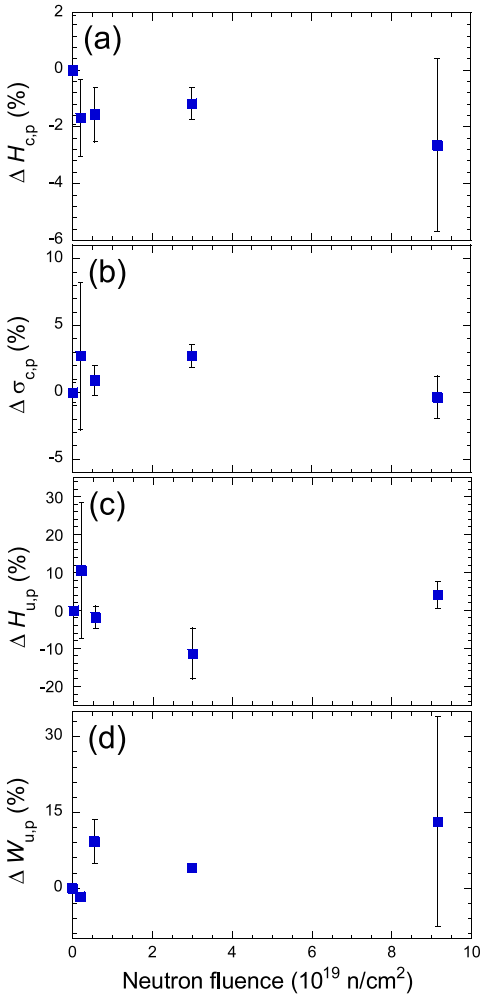

Figure 7: Neutron fluence dependence of (a) peak position and (b) width parameter of $\rho_{\rm c}(H_{\rm c})$, and (c) peak position and (d) width parameter of $\rho_{\rm u}(H_{\rm u})$, for the LJ sample.

in a Fe matrix. If Cu atoms are homogeneously distributed in the sample, distance between adjacent Cu atoms would be ~ 1 nm. Since the distance is much smaller than a domain wall width, the domain walls may displace in a matrix, without the pinning at Cu atom sites creating local lattice strain. Under neutron irradiation, Cu atoms segregate and form precipitates through irradiation-enhanced diffusion process. Since a Cu-rich precipitate creates a stress field around it [32], a stress field in a matrix becomes inhomogeneous; the stress field around the precipitates develops with their growth whereas it decreases in the other matrix region due to the reduced number of dissolved Cu atoms. Therefore the pinning effect on the Bloch wall movement enhances at around the precipitates in particular. Note that assuming the number density and size of nanoscale features (Cu-rich precipitates) listed in Table 3 and their homogeneous distribution, the distance between neighboring Cu-rich precipitates would be ~ 28 and 17 nm for Irrad-3 and Irrad-4, respectively; such distance may be enough

for Bloch walls to feel the spatial variation of stress fields in a matrix. The increased magnetic inhomogeneity in a matrix leads to an increase of the coercivity distribution $\sigma_{\mathrm{c,p}}$ shown in Fig. 7(b).

Finally, we remark the peak position of $\rho_{\mathrm{u}}(H_{\mathrm{u}})$ along the H_{u} axis. If there exist magnetic regions with different coercivity, each magnetic region feels interaction fields from the surrounding magnetic regions during magnetization process. For instance, when external magnetic field is reduced from a positive high field, magnetically softer regions without Cu precipitates would preferentially reverse their magnetization. However, the magnetization reversal may be influenced by magnetostatic interaction fields, coming from the adjacent magnetically harder regions. Such interaction field results in the broadening of the $\rho_{\mathrm{u}}(H_{\mathrm{u}})$ peak along the H_{u} axis [17] and may be responsible for the increase of $W_{\mathrm{u,p}}$ after neutron irradiation shown in Fig. 7(d). The interaction fields, on the other hand, shift the position of $\rho_{\mathrm{u}}(H_{\mathrm{u}})$ along the H_{u} axis, whose direction depends on whether the interaction field acts as a demagnetizing or magnetizing field [17, 33]. Considering the negative value of $H_{\mathrm{u,p}}$ shown in Fig. 7(c), positive magnetostatic interactions may exist between magnetic regions with and without Cu-rich precipitates. Further systematic FORC studies for RPV model alloys with variable Cu, Ni, and Mn, which are key elements of precipitation hardening are in progress to get in-depth information about nanoscale precipitation and FORC parameters.

4. Summary

We performed measurements of major hysteresis loops and FORCs for A533B-type RPV model alloys with variable Cu contents (0.0−0.42 wt% Cu), subjected to neutron irradiation up to a fluence of 9×10^{19} n cm^{-2}. The major-loop coercivity exhibits a local maximum in the low fluence regime and then decreases at higher fluence for all the samples. The appearance of the maximum can be due to the competition between the formation of nanoscale defects and recovery, which increase and decrease coercivity, respectively. The decrease in coercivity at the highest fluence is larger for the high-Cu sample, indicating that magnetic softening due to recovery is enhanced for the high-Cu sample. On the other hand, FORCs, which consist of many hysteresis curves with different reversal fields, give much information about coercivity distribution and interaction field between magnetic regions. From the FORC analysis for the high-Cu sample, we found that a position of the FORC distribution peak shifts towards a lower coercivity just after irradiation, then move to the higher coercivity at medium fluence. This behavior may reflect the competing microstructural changes. At the same time, the FORC distribution peak exhibits the broadening after irradiation, along both the coercivity and interaction field axes. This broadening can be attributed to the increase in magnetic inhomogeneity due to the Cu precipitation, leading to the enhancement of the magnetostatic interaction between magnetic regions with different coercivity. These findings demonstrate that FORCs can be a power tool to provide the in-depth information about local magnetic features, which can not be obtained by conventional hysteresis measurements.

Acknowledgements

The part of this work was performed under the Inter-University Cooperative Research Program of the International Research Center for Nuclear Materials Science, Institute for Materials Research, Tohoku University, (Proposal No. 17M0001, 18M0001, 19M0003, 20M0002). This work was supported by Grant-in-Aid for Scientific Research (B) (Grant No. 25289346, 19H02640) from JSPS, Japan. The part of this work was supported by JSPS and Hungarian Academy of Science under the Japan - Hungary Research Cooperative Program. The SANS experiments were based upon experiments performed at the KWS-1 instrument operated by JCNS at the Heinz Maier-Leibnitz Zentrum (MLZ), Garching, Germany (Proposal No. 12748). We acknowledge supports from FRM II radiation protection for assistance in SANS experiments on irradiated materials.

Data Availability

The raw/processed data required to reproduce these findings can not be shared at this time as the data form a part of an ongoing study.

References

[1] G. R. Odette, T. Yamamoto, T. J. Williams, R. K. Nanstad, and C. A. English, On the history and status of reactor pressure vessel steel ductile to brittle transition temperature shift prediction model, J. Nucl. Mater. **526** (2019) 151863.

[2] P. B. Wells, T. Yamamoto, B. Miller, T. Milot, J. Cole, Y. Wu, and G. R. Odette, Evolution of manganese-nickel-silicon-dominated phases in highly irradiated reactor pressure vessel steels, Acta Mater. **80** (2014) 205-219.

[3] M. Blaszkiewicz, The development of nondestructive evaluation (NDE) for monitoring the embrittlement in nuclear reactor pressure vessels, Mater. Sci. Forum **210 – 213** (1996) 9-16.

[4] V.I. Frankfurt and D.S. Kupperman, Review of electromagnetic NDT methods for monitoring the degradation of nuclear reactor components, Mater. Eval. **59** (2001) p.1053.

[5] H. Kronmüller, M. Fähnle, Micromagnetism and the microstructure of ferromagnetic solids, Cambridge University press, Cambridge, 2003.

[6] D. C. Jiles, Magnetic properties and microstructure of AISI 1000 series carbon steels, J. Phys. D: Appl. Phys. **21** (1988) 1186-1195.

[7] E. S. Gorkunov, V. M. Somova, T. P. Tsar'kova, S. S. Rodionova, I. A. Kuznetsov, and L. D. Gavrilova, Relationship of coercivity to the chemical composition and microstructure of annealed steels, Russ. J. Nondestruct. Test. **33** (1997) 544-559.

[8] J.F. Stubbins, W.J. Shong, M. Giacobbe, A.M. Ougouag, J.G. Williams, Pressure vessel steel embrittlement monitoring by magnetic properties measurements, ASTM STP **1204** (1993) 5-15.

[9] M.K. Devine, D.C. Jiles, P.K. Liaw, R.D. Rishel, D.S. Drinon, Magnetic properties changes in various structural steels due to radiation, Rev. Prog. Quantitative NDE **12** (1993) 1815-1822.

[10] S.-H. Chi, K.-O. Chang, J.-H. Hong, I.-H. Kuk, and C.-O. Kim, Changes in magnetic parameters of neutron irradiated SA 508 C.3 reactor pressure vessel forging and weld surveillance samples, J. Appl. Phys. **85** (1999) 6043-6045.

[11] D.G. Park, C.G. Kim, H.C. Kim, J.H. Hong, I.S. Kim, Effect of neutron irradiation on magnetic properties in the low alloy Ni-Mo steel SA508-3, J. Appl. Phys. **81** (1997) 4125-4127.

[12] S. Takahashi, S. Kobayashi, H. Kikuchi, and Y. Kamada, Relationship between mechanical and magnetic properties in cold rolled low carbon steel, J. Appl. Phys. **100** (2006) 113908.

[13] S. Kobayashi, S. Takahashi, T. Shishido, Y. Kamada, and H. Kikuchi, Low-field magnetic characterization of ferromagnets using a minor-loop scaling law, J. Appl. Phys. **107** (2010) 023908.

[14] S. Kobayashi, H. Kikuchi, S. Takahashi, Y. Kamada, K. Ara, T. Yamamoto, D. Klingensmith, and G.R. Odette, Neutron irradiation effects on magnetic minor hysteresis loops in nuclear reactor vessel steels, Philos. Mag. **88** (2008) 1791-1800.

[15] S. Kobayashi, H. Kikuchi, S. Takahashi, Y. Kamada, K. Ara, T. Yamamoto, D. Klingensmith, and G.R. Odette, The effect of copper and manganese on magnetic minor hysteresis loops in neutron irradiated Fe model alloys, J. Nucl. Mater. **88** (2009) 109-114.

[16] S. Kobayashi, T. Yamamoto, D. Klingensmith, G.R. Odette, H. Kikuchi, and Y. Kamada, Magnetic evaluation of irradiation hardening in A533B reactor pressure vessel steels: Magnetic hysteresis measurements and the model analysis, J. Nucl. Mater. **422** (2012) 158-162.

[17] A. P. Roberts, D. Heslop, X. Zhao, and C. R. Pike, Understanding fine magnetic particle systems through use of first-order reversal curve diagrams, Rev. Geophys. **52** (2014) 557-602.

[18] K. Miyazawa, S. Okamoto, T. Yomogita, N. Kikuchi, O. Kitakami, K. Toyoki, D. Billington, Y. Kotani, T. Nakamura, T. Sasaki, T. Ohkubo, and K. Hono, First-order reversal curve analysis of a Nd-Fe-B sintered magnet with soft X-ray magnetic circular dichroism microscopy, Acta Mater. **162** (2019) 1-9.

[19] B.C. Dodrill, J. Lindemuth, C. Radu, H. Reichard, High-temperature FORC study of single- and multi-phase permanent magnets, MRS Bulletin **40** (2015) 903-904.

[20] S. Kobayashi, H. Murakami, A. Horvath, L. Almasy, F. Gillemot, A. Feoktystov, Effects of neutron irradiation on magnetic first-order reversal curves in reactor pressure vessel steels, AIP Adv. **10** (2020) 015221.

[21] G. R. Odette, G. E. Lucas, D. Klingensmith, B. D. Wirth, D. Gragg, The Effects of Composition and

Heat Treatment on Hardening and Embrittlement of Reactor Pressure Vessel Steels, NUREG/CR-6778 (U.S. Nuclear Regulatory Commission, Washington, DC, 2003).
[22] A.V. Feoktystov, H. Frielinghaus, Z. Di, S. Jaksch, V. Pipich, M.-S. Appavou, E. Babcock, R. Hanslik, R. Engels, G. Kemmerling, H. Kleines, A. Ioffe, D. Richter, and T. Brückel, KWS-1 high-resolution small-angle neutron scattering instrument at JCNS: current state, J. Appl. Cryst. **48** (2015) 61-70.
[23] H. Frielinghaus, A. Feoktystov, I. Berts, and G. Mangiapia, KWS-1: Small-angle scattering diffractometer, Journal of large-scale research facilities **1** (2015) A28.
[24] J. Ilavsky, P.R. Jemian, Irena: tool suite for modeling and analysis of small-angle scattering, J. Appl. Cryst. **42** (2009) 347-353.
[25] A. Michels, Magnetic small-angle neutron scattering of bulk ferromagnets, J. Phys.: Condens. Matter **26** (2014) 383201.
[26] K. Osamura, H. Okuda, M. Takashima, K. Asano, and M. Furusaka, Small-angle neutron scattering study of phase decomposition in Fe-Cu binary alloy, Mater. Trans. JIM **34** (1993) 305-311.
[27] E. D. Eason, G. R. Odette, R. K. Nanstad, and T. Yamamoto, A Physically Based Correlation of Irradiation-Induced Transition Temperature Shifts for RPV Steels, Oak Ridge National Laboratory Report ORNL/TM-2006/530, 2007.
[28] G. R. Odette, T. Yamamoto, and D. Klingensmith, On the effect of dose rate on irradiation hardening of RPV steels, Philos. Mag. **85** (2005) 779-797.
[29] S. Kobayashi, H. Sato, T. Iwawaki, T. Yamamoto, D. Klingensmith, G.R. Odette, H. Kikuchi, and Y. Kamada, Effect of long-term thermal aging on magnetic property in reactor pressure vessel steels, J. Nucl. Mater. **439** (2013) 131-136.
[30] M. Saleh, Y. Cao, D. J. Edwards, P. Ramuhalli, B. R. Johnson, and J. S. McCloy, Effects of aging time and temperature of Fe-1wt.%Cu on magnetic Barkhausen noise and FORC, AIP Adv. **6** (2016) 055935.
[31] S. Kobayashi, R. Kawagoe, H. Murakami, K. Ohishi, Y. Kawamura, and J. Suzuki, Thermal aging effects on magnetization reversals in a pre-deformed Fe-1wt%Cu alloy studied via first-order reversal curves, Philos. Mag. Lett. **99** (2019) 217-225.
[32] S. Y. Hu, Y. L. Li, and K. Watanabe, Calculation of internal stresses around Cu precipitates in the bcc Fe matrix by atomic simulation, Modelling Simul. Mater. Sci. Eng. **7** (1999) 641-655.
[33] D. A. Gilbert, G. T. Zimanyi, R. K. Dumas, M. Winklhofer, A. Gomez, N. Eibagi, J. L. Vicent, and K. Liu, Quantitative decoding of interactions in tunable nanomagnet arrays using first order reversal curves, Sci. Rep. **4** (2014) 4204.